Magnetolattice coupling, magnetic frustration, and magnetoelectric effect in the Cr-doped $FeVO_4$ multiferroic material and their correlation with structural phase transitions

Ganesh Bera,[1] Akash Surampalli,[2] Aradhya Mishra,[1] P. Mal,[1] V. R. Reddy,[2] A. Banerjee,[2] Archna Sagdeo,[3,4] Pradip Das,[1] and G. R. Turpu[1,*]

[1]*Department of Pure and Applied Physics, Guru Ghasidas Vishwavidyalaya, Bilaspur 495009, India*
[2]*UGC-DAE CSR, University Campus, Khandwa Road, Indore 452001, India*
[3]*Synchrotrons Utilization Section, Raja Ramanna Centre for Advanced Technology, Indore 452017, India*
[4]*Homi Bhabha National Institute, Training School Complex, Anushakti Nagar, Mumbai 400094, India*

(Received 16 April 2019; revised manuscript received 4 July 2019; published 29 July 2019)

A detailed account of magnetolattice coupling, magnetic frustration, and magnetoelectric effects in $Fe_{1-x}Cr_xVO_4$ ($x = 0 - 1.0$) studied by temperature-dependent synchrotron x ray diffraction (SXRD), temperature- and magnetic-field-dependent dielectric permittivity ε, and magnetization measurements are presented in this paper where progressive Cr doping leads to structural transitions from triclinic (T)—monoclinic (M)—orthorhombic (O) symmetries. SXRD data shows an intricate relationship between magnetic, ferroelectric, and lattice degrees of freedom in these systems. $FeVO_4$ reaches a magnetically ordered state with two successive antiferromagnetic orderings at T_{N1} (21.85 K) and T_{N2} (15.65 K), having collinear and noncollinear natures, respectively, as evidenced in DC magnetization measurements. Progressive Cr^{3+} incorporation at the Fe^{3+} site in $Fe_{1-x}Cr_xVO_4$ shifts these transitions to higher temperatures in T phase ($x = 0.0$ and 0.10). At $x = 0.175$ [in (T + M) phase], these transitions become closer to each other. Beyond this concentration, a single broad antriferromagnetic transition is observed in M ($x = 0.20 - 0.30$) and O ($x = 0.90 - 1.0$) phases. A nonlinear behavior in isotherm M-H curves below T_{N2} indicates field-induced spin-reorientation transitions at higher magnetic field. In dielectric permittivity ε a sharp peak at T_{N2} in T and near M regions with a minimal suppression because of applied magnetic field is found and no such peak is observed in far M phase. A discontinuity evidenced in electromagnetic susceptibility indicates magnetoelectric effect at the polar to nonpolar transition regions. The structural incongruence in progressive transformation from T to M to O symmetries plays a vital role in controlling the nature of magnetic interactions. Our results indicate a strong correlation between structural transitions, magnetolattice coupling, magnetic frustrations, and magnetoelectric effect in $Fe_{1-x}Cr_xVO_4$.

DOI: 10.1103/PhysRevB.100.014436

I. INTRODUCTION

Multiferroic materials exhibiting more than one ferroic order such as (anti)ferromagnetism and ferroelectricity (FE) hold great potential for applications due to magnetoelectric (ME) coupling, allowing switching of improper ferroelectricity associated with magnetic field and vice versa. The contradicting requirements for mutiferroicity are the presence of *d* electrons for magnetism, where ferroelectric distortion is suppressed by the presence of *d* electrons and FE needs the crystallization in a noncentrosymetric space group, producing an acentric frustrated magnetic structure that breaks the inversion symmetry of the lattice [1–5]. Several multiferroic materials have been studied wherein the FE arises due to various reasons [5–11]. Amongst available multiferroics, type-II multiferroics exhibit ferroelectric nature induced by a magnetically ordered phase where the cross coupling between two ferroic orders may lead to the ME effect, such as polarization switching in the materials due to spiral spin order with external magnetic fields [10–12]. The magnetically induced FE in type-II multiferroics has several different microscopic mechanisms in different types of materials. One of the most common origins is the breaking of space inversion symmetry having a noncollinear spiral spin order where the FE is driven by inverse Dzyaloshinskii-Moriya (IDM) interaction associated with relativistic spin-orbit exchange interactions. This type of polarization is formulated as $P \sim e_{ij} \times (S_i \times S_j)$, where e_{ij} is the unit vector connecting two neighboring spins, S_i and S_j, which can be arising from spin currents, ionic displacement, or induced polar lattice distortions [11–14]. Some well-studied examples having this type of origin are $DyMnO_3$ [15], $TbMnO_3$ [16], $Ni_3V_2O_8$ [17], YMn_2O_5 [18], and $MnWO_4$ [19,20], where the polarization switching is driven by an external magnetic field, leading to a ME effect [21]. Another common origin of improper FE in type-II multiferroics having collinear magnetic spin structure is exchange striction or magnetostriction without spin-orbit interaction, where the FE polarizations can be expressed as $P \sim S_i.S_j$ [11–14,22,23]. This type of mechanism occurs either in the presence of different transition metal (TM) ions or in the same TM ions with different charge states, as can be seen in $Ca_3Co_{1-x}Mn_xO_6$ or Ca_3CoMnO_6 [9,24] RMO_3 (R = Gd, Ho, Sm and M = Fe, Mn) [25–28]. The spin-dependent *p-d* hybridization also causes a small electrical polarization as evidenced in multiferroic $Ba_2CoGe_2O_7$ material [29] in which the polarization is given

*Corresponding author: dr.tgreddy@gmail.com

by $P \sim (S_i.e_{il})^2 e_{il}$ where e_{il} is the vector connecting the S_i and the neighbor ligand ions [11–14]. Recently, a mechanism of the ME with a microscopic origin in spin currents has been floated theoretically and is directly related with the noncollinear or spiral spin structure [30]. The spin current, i.e., interaction between a localized magnetic moment and spin angular momentum flow plays a central role in controlling the spintronic devices, taking into account the spin-orbit interactions which can produce the electric polarization in noncentrosymmetric systems. This is a recent topic of research in the field of condensed-matter physics, to study the generation as well as the detection of spin current in materials due to its potential for device applications in spintronics [31–33].

$FeVO_4$ is identified as a multiferroic system having triclinic (T) symmetry with *P-1* space group [34], having a chainlike structure built from Fe-O polyhedrals, where Fe^{3+} ions occupy three distinct crystallographic sites, two FeO_6 octahedra and one FeO_5 trigonal bipyramid separated by three VO_4 groups in its lattice. $FeVO_4$ falls under the type-II multiferroic materials category, having improper FE driven by spiral magnetic order. Magnetization and specific heat studies on polycrystalline and single-crystal specimens of $FeVO_4$ revealed two distinct antiferromagnetic (AFM) transitions around $T_{N1} = 22$ K and $T_{N2} = 15$ K [35–37]; the nature of the transitions was confirmed by neutron diffraction studies on polycrystalline samples to be a collinear incommensurate AFM and a noncollinear incommensurate or spiral AFM order, respectively [38]. Usually, the emergence of noncollinearity is due to antisymmetric spin-orbit coupling of Dzyaloshinskii-Moriya-type interactions, which produces the magnetically induced FE. $FeVO_4$ is distinguished as a unique type-II multiferroic which challenges the mechanism of multiferroic theories because there is simultaneous breaking of inversion symmetry of magnetic order in both the magnetic transitions (T_{N1} and T_{N2}), but FE appears only below T_{N2} associated with spiral magnetic ordering. Hence, the validity of IDM interactions in this case is questionable, and there are theoretical arguments that magnetic movement reduction or spin-rotation of the acentric spiral magnetic phase in the form of spin current could be a reason for this simultaneous occurance of FE and spiral order at T_{N2} in $FeVO_4$ [38]. The correlation between magnetostriction and magnetopolarization effect have also been identified with a dominating contribution of magnetoelasticity in the observed ME coupling [35].

The chemical doping of $FeVO_4$ significantly affects the structural, magnetic, and electrical properties due to the variation in the interaction strengths of the magnetic coupling [39]. $Fe_{1-x}Cr_xVO_4$ solid solutions have been studied by Attfield *et al.* [40] many years ago. They reported the crystal and magnetic structures of these solid solutions ($x = 0.25$, 0.50, and 0.75), presenting that the magnetic frustration increases with the increase of Cr^{3+} content corresponding to increasing amounts of short-range magnetic order. Recently, Cr^{3+} (magnetic ion)-doped $FeVO_4$ was studied to understand the nature of multiferroicity [39]. Our recent results on a series of samples in $Fe_{1-x}Cr_xVO_4$ system with 16 different concentrations manifested a detailed structural phase diagram of these materials [41]. In view of our recent results, here we present a detailed study on the nature of magnetolattice coupling, magnetic frustration, and ME coupling in $Fe_{1-x}Cr_xVO_4$ ($x = 0.0 - 1.0$) through detailed SXRD, magnetic, and dielectric studies supported by detailed analysis.

II. EXPERIMENTAL METHODS

Polycrystalline $Fe_{1-x}Cr_xVO_4$ ($0 \leqslant x \leqslant 1.0$) solid solutions were synthesized by standard solid-state reaction method. The synthesis and structural analysis details were described in one of our previous reports [41]. The temperature-dependent SXRD of $Fe_{1-x}Cr_xVO_4$ ($x = 0.0$, 0.10, 0.175, and 0.30) was performed by using a 12.52-keV ($\lambda = 0.990084$ Å) synchrotron x-ray source, recorded using an image plate (Mar 345) area detector at angle dispersive x ray diffraction beamline (BL-12), Indus-2, RRCAT, Indore. The measurements were taken over a range of temperatures from 5 K to 50 K, i.e., across the transition temperature and at room temperature (300 K) as well. The temperature of the sample was controlled by a liquid He-based flow-type cryostat in the low-temperature experiment. All the SXRD data were converted into 2θ format using FIT2D software after calibrating the data using LaB_6 SXRD data as standard. The DC-magnetization measurements were carried out using Quantum Design 16 T PPMS-VSM system in the temperature range of 5–300 K at 500 Oe external magnetic field for all the reported compounds of solid solutions. The temperature and magnetic-field-dependent dielectric studies were carried out by using a computer-programming (Visual Basic)-controlled KEYSIGHT E4980A precision LCR meter (20 Hz–2 MHz) and the measurements were done over a range of frequencies at excitation of 1 V. Here the temperature was swept at a very slow warming and cooling rate (0.2 K and 0.5 K/min) for all the taken samples (pellets) in a parallel plate geometry having electrodes fashioned from silver paste within Janis-made superconducting magnet using a homemade sample holder.

III. RESULTS AND DISCUSSION

A. Temperature-dependent SXRD study

Figures 1(a)–1(d) depict the temperature-dependent SXRD patterns of $Fe_{1-x}Cr_xVO_4$ ($x = 0.0$, 0.1, 0.175, and 0.30), where $x = 0.0$ and 0.1 are in T, $x = 0.175$ is in [T + monoclinic (M)], and $x = 0.30$ is in M crystal structures, respectively. Profile fitting of the experimental data was performed by Le Bail method using FULLPROF software. The crystal symmetry of the samples remains the same down to 5 K. The inset of Figs. 1(a)–1(d) highlight the characteristic diffraction peaks of selected 2θ range at different temperatures for specific crystal structures where there is a variation in the peak position with temperature. Three distinct regions of solid solution corresponding to T, (T+M), and M phases are discussed separately to understand coupling between structure and magnetic/electric orders as a function of temperature.

1. $Fe_{1-x}Cr_xVO_4$ *($x = 0.0$ and 0.10) triclinic phase*

The diffraction patterns for $x = 0.0$ and 0.10 as shown in Figs. 1(a) and 1(b) are refined using the *P-1* space group to evaluate the lattice parameters. The variation of structural parameters with temperature is shown in Figs. 2(a)–2(f), 3(a)–3(f), and Figs. S1(a) and S1(b) (Supplemental Material

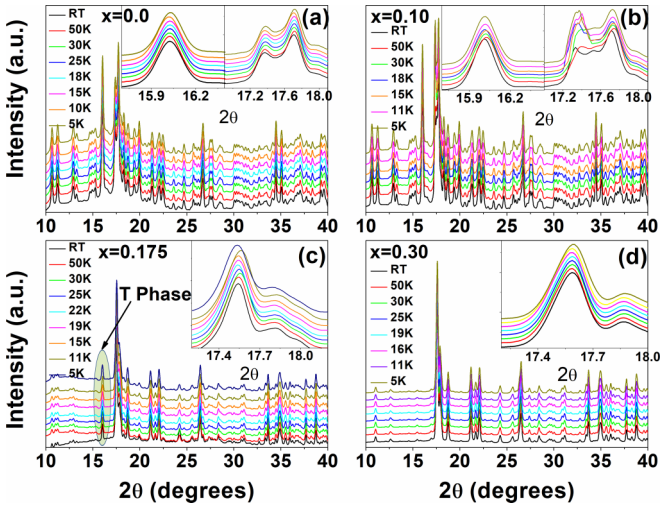

FIG. 1. Temperature-dependent SXRD patterns at the temperature range 5–50 K and at 300 K of $Fe_{1-x}Cr_xVO_4$ (a), (b) $x = 0.0$, 0.1, (c) 0.175, and (d) 0.30 corresponding to triclinic (T), [T + monoclinic (M)], and M structures, respectively.

[42]) for the two samples, respectively. It is observed that the lattice constants a, b, c, α, β, γ, and unit cell volume V increase with temperature due to lattice expansion. Two sharp changes in lattice parameters and volume are observed across the magnetic phase transitions (at T_{N1} and T_{N2}) as shown in Figs. 2(a)–2(f), 3(a)–3(f), and Figs. S1(a) and S1(b) (Supplemental Material [42]) by dashed lines. The variation of lattice distortion factors as a function of temperature are illustrated in Figs. S2(a) and S2(b) (Supplemental Material [42]) for $x = 0.0$ and $x = 0.10$. Two anomalies are observed in lattice distortion factors (a/c and b/c) like lattice parameter variations at magnetic transitions. These two anomalies in

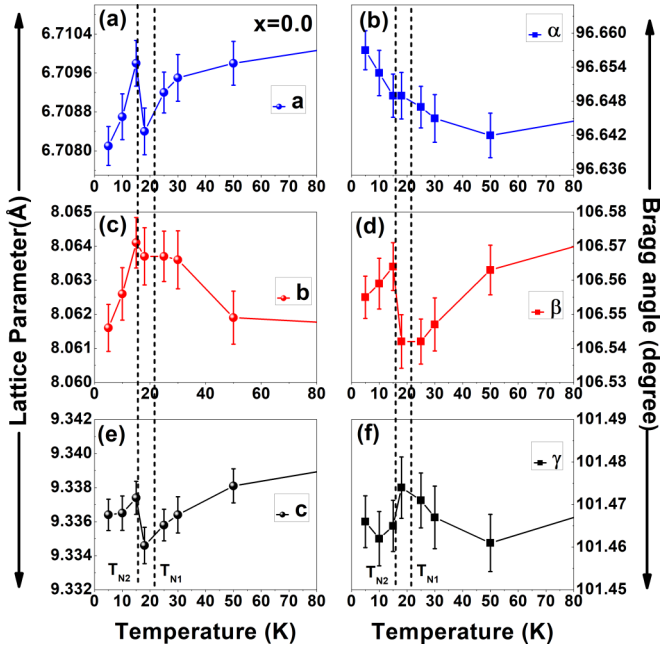

FIG. 2. The lattice parameters as a function of temperature of polycrystalline $Fe_{1-x}Cr_xVO_4$ solid solutions for $x = 0.0$ (a), (c), (e) lattice constants a, b, c and (b), (d), (f) Bragg's angles α, β, γ.

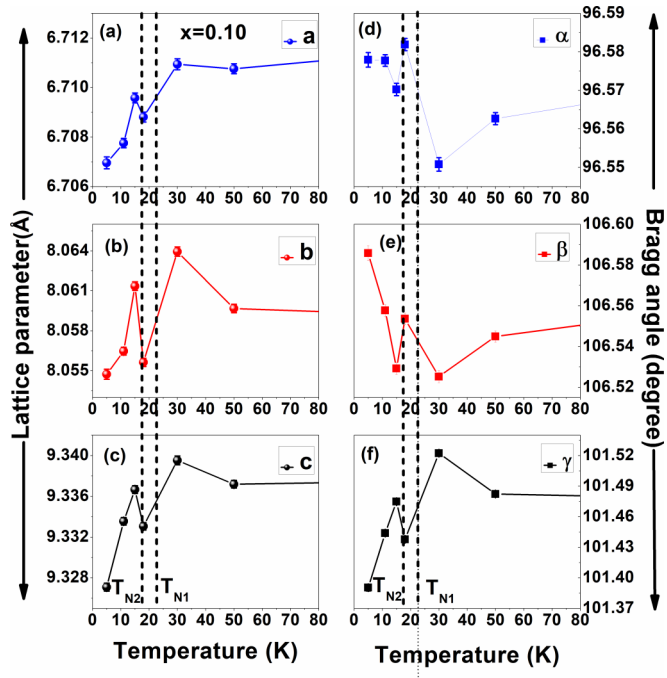

FIG. 3. The variation of lattice parameters with temperature of polycrystalline $Fe_{1-x}Cr_xVO_4$ solid solutions for $x = 0.10$ (a)–(c) lattice constants a, b, c and (d)–(f) Bragg's angles α, β, γ.

this system suggest a strong correlation between structure magnetic/electric polarization that happens at these temperatures. With Cr incorporation at Fe site, the anomalies of lattice constants are shifted slightly toward higher temperature, corresponding to magnetic transitions. Therefore, the lattice anomalies around the transition temperatures at T_{N1} and T_{N2} are direct evidence of magnetolattice coupling in these systems.

2. $Fe_{0.825}Cr_{0.175}VO_4$ *(triclinic + monoclinic) phase*

Rietveld analysis of SXRD patterns for $x = 0.175$ is done using $C2/m$ space group (M phase), which is the dominant phase in the specimen, over 5–300 K temperature range where a very small amount of residual phase (T phase) is present in the system which is seen in Fig. 1(c) and highlighted. The temperature dependence of the lattice constants a, b, c, β, and unit cell volume V at low temperature are shown in Figs. 4(a)–4(d) and Fig. S1(c) (Supplemental Material [42]), respectively. Anomalies in the crystal lattice parameter plot are clearly observed at T_{N1}, T_{N2}, and at T_{NR}, corresponding to the magnetic phase transitions where T_{NR} is considered as the transition temperature due to residual T phase. Similar behavior is observed in lattice distortion factors (a/c and b/c) also, as shown in Fig. S2(c) (Supplemental Material [42]). A sluggish and nontrivial presence of anomalies in this sample in the vicinity of T_{N1}, T_{N2}, and at T_{NR} is clear evidence that the crystal lattice goes through various changes, indicating a strong coupling between lattice-magnetic/electric degrees of freedom.

3. $Fe_{1-x}Cr_xVO_4$ *($x = 0.30$) monoclinic phase*

The SXRD data for $x = 0.30$ was fitted by Rietveld refinement using $C2/m$ space group of pure M phase. The variation

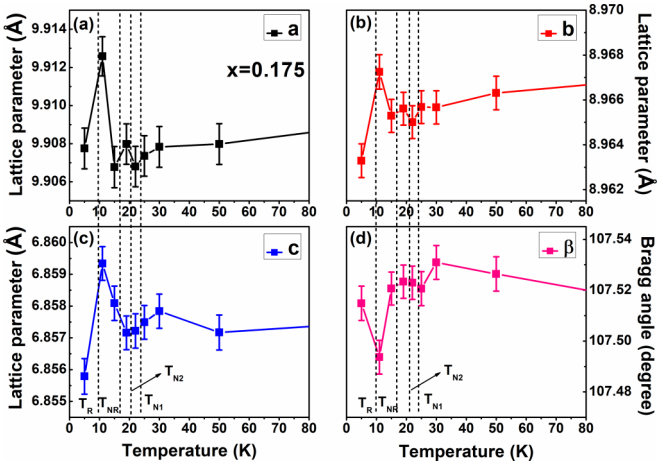

FIG. 4. Temperature-dependent lattice constants of polycrystalline $Fe_{1-x}Cr_xVO_4$ solid solutions for $x = 0.175$, (a)–(d) lattice constants a, b, c, and Bragg's angle β, respectively.

of lattice parameters a, b, c, β, and unit cell volume V at low temperature are illustrated in Figs. 5 and S1(d) (Supplemental Material [42]), respectively. It is observed that lattice constants change around T_N, corresponding to a magnetic transition with a broad temperature range, indicating magnetolattice coupling. The small changes in lattice distortion factors (a/c and b/c) is seen at T_N, shown in Fig. S2(d) (Supplemental Material [42]). Also, another sharp change at low temperature below 10 K is seen in the lattice constant variation, suggesting spin-lattice coupling due to weak ferromagnetism at low temperature.

B. Magnetic frustration in $Fe_{1-x}Cr_xVO_4$

1. DC magnetization studies

To investigate the magnetic transitions and the effect of Cr doping on these transitions in $FeVO_4$, temperature- and field-dependent DC magnetization measurements were carried out under zero-field-cooled (ZFC) and field-cooled (FC) protocols at an applied external magnetic field of 500 Oe over a temperature range of 5–300 K. The isotherm M-H measurements were

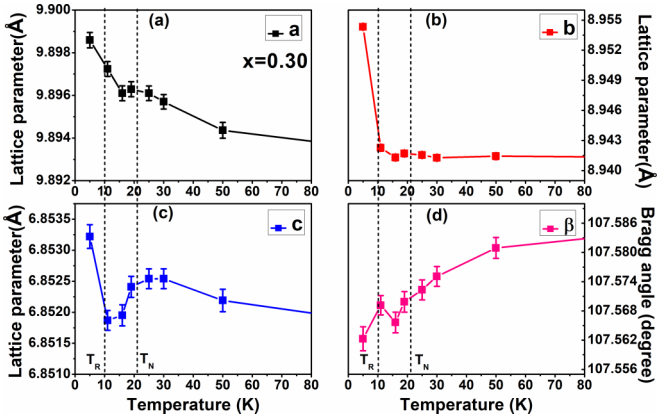

FIG. 5. Temperature variation in lattice constants of polycrystalline $Fe_{1-x}Cr_xVO_4$ solid solutions for $x = 0.30$, (a)–(d) lattice constants a, b, c, and Bragg's angle β, respectively.

carried out with high applied magnetic field up to 16 T. To calculate the magnetic parameter temperature-dependent $\chi^{-1}(T)$ plot of $Fe_{1-x}Cr_xVO_4$ ($0 \leqslant x \leqslant 1.0$), solid solutions were done and fitted with the paramagnetic Curie-Weiss law in the paramagnetic region above 120 K. The effective paramagnetic moments per formula unit were determined using the relation $\mu_{\text{eff}} = \sqrt{8C}$, where C = 1/slope of the $\chi^{-1}(T)$ plot is the paramagnetic Curie constant [43]. The magnetic frustration factor (f) of $Fe_{1-x}Cr_xVO_4$ ($0 \leqslant x \leqslant 1.0$) is calculated using the relation $f = |\theta_w| / T_N$, where θ_w is the paramagnetic Curie-Weiss temperature and T_N is the Neel temperature of corresponding compositions [44]. Detailed analysis of magnetization studies have been done separately for different crystal symmetries as given in the following subsections.

(a) $Fe_{1-x}Cr_xVO_4$ *($x = 0.0$ and 0.10) triclinic phase.* Figures 6(a)–6(c) show the temperature-dependent magnetization (M-T) and M-H data of the $Fe_{1-x}Cr_xVO_4$ ($x = 0.0$, 0.10). ZFC and FC curves overlap each other and the nature of magnetic transitions are AFM for both $x = 0.0$ and $x = 0.10$ systems. There are two sharp long-range magnetic orderings [45] in $FeVO_4$ at 21.85 K (T_{N1}), which is collinear AFM, and at 15.65 K (T_{N2}), which is noncollinear or spiral AFM in confirmity with existing literature. The measured effective paramagnetic moments per formula unit and the paramagnetic Weiss temperatures (θ_w) of $Fe_{1-x}Cr_xVO_4$ ($0 \leqslant x \leqslant 1.0$) are given in the Table I. The values of the Weiss temperatures with negative signs indicate a strongly frustrated AFM ordering [46]. It is clearly observed that the effective moment (μ_{eff} in μ_B) and magnetic frustration factor slightly increases for $x = 0.10$ due to dominant d^5-d^5 (Fe-O-Fe) interactions as shown in Figs. S3(a) and S3(b) (Supplemental Material [42]).

The M-H curves clearly show gradual increase in magnetization with the applied magnetic field without showing any signature of saturation up to the highest magnetic field (16 T), indicating robust and frustrated AFM ordering. In the $x = 0.10$ system, the transition temperatures were observed to move toward higher temperatures and the net magnetization also decreases. For $x = 0.0$, the M-H measurements are taken at 5 K, 10 K, and 20 K temperatures and at 5 K and 20 K for $x = 0.10$. The M-H curve shows linear behavior at 20 K (above T_{N2}) for both cases without any saturation up to highest magnetic field where the magnetization increases with increasing temperature, characteristic of AFM materials [47]. The nonlinearity in M-H curves is identified at 5 K and 10 K for $x = 0.0$ and at 5 K for $x = 0.10$ (below T_{N2}) as can be seen in the inset of Figs. 6(b) and 6(c) with dM/dH curves. It is clearly observed that the noncollinear or spiral magnetic order is influenced by the external applied magnetic field and a field-induced spin reorientation or spin-flop transition is found above 3 T with a broad range from 3 T to 5.4 T [48]. This seems to be a noncollinear transition which produces a ferroelectric ordering (T_{N3}) below T_{N2} as can be seen in Sec. III C.

(b) $Fe_{0.825}Cr_{0.175}VO_4$ *(triclinic + monoclinic) phase.* Figures 7(a) and 7(b) depict the temperature-dependent magnetization (M-T) and M-H data of the $Fe_{1-x}Cr_xVO_4$ ($x = 0.175$). In this system, a dominant M phase coexists with small residual T phase. Interestingly, three magnetic transitions are observed in the M-T curve at 23.03 K, 21.05 K, and 17.02 K as shown in the inset of Fig. 7(a) with dM/dT curve. It is almost

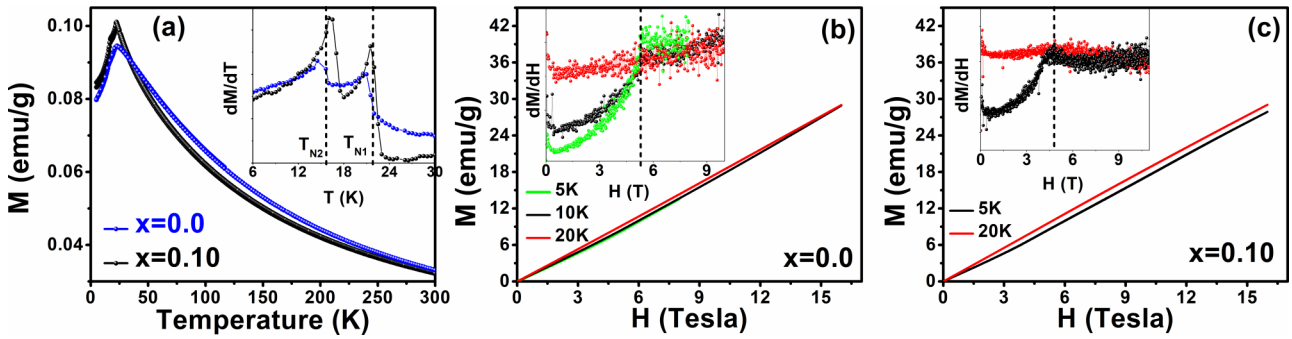

FIG. 6. Magnetizations as a function of temperature at 500 Oe applied field of polycrystalline $Fe_{1-x}Cr_xVO_4$ solid solutions (a) $x = 0.0 - 0.10$ and magnetization as a function of applied magnetic field (b) $x = 0.0$, (c) $x = 0.10$. The inset in (a) illustrates the first derivatives of M-T curves to find the exact Neel temperatures and in (b), (c) shows dM/dH to confirm nonlinearity.

impossible for us to conclude whether there is one more magnetic transition hidden in the second broad peak. The effective paramagnetic moment per formula unit and magnetic frustration factor (f) were deduced from χ^{-1}(T) plot, shown in Fig. S3(c).

It is found that the effective moment decreases due to the average of all possible interactions like d^5-d^5, d^5-d^3, and d^3-d^3 interactions, due to Fe-O-Fe, Fe-O-Cr, and Cr-O-Cr exchange interaction respectively. The magnetic frustration factors increase due to emergence of short-range magnetic ordering. A linear M-H curve is observed at 22 K (above T_{N2}) and nonlinear behavior is identified at 5 K between 3 T to 5 T fields and it merges with the linear curve above 5 T, revealing the field-induced magnetic transition (T_{N3}) occurs below T_{N2}, which is also a noncolliear which induces an additional ferroelectric transition, as seen in dielectric studies.

(c) $Fe_{1-x}Cr_xVO_4$ *($x = 0.20$ and 0.30) monoclinic phase.* With further increase in Cr^{3+} content, the two transitions get merged into one broad transition at 22.55 K and 21.03 K for $x = 0.2$ and $x = 0.3$, respectively, shown in Fig. 8(a). It is also observed that there is some up turn in magnetic moment in M-T curves around 9 K and 10 K, for $x = 0.20$ and 0.30, respectively, indicating the presence of weak ferromagnetic interactions corresponding to some magnetic reorientation at low temperatures, generated by dominating Fe^{3+}-O-Cr^{3+} interactions according to Goodenough-Kanamori-Anderson (GKA) rules (explained in the Appendix) of superexchange (SE) interactions [49–51]. It is clearly observed that th effective moment (μ_{eff} in μ_B) decreases for $x = 0.20$ and $x = 0.30$ where there is a change in crystal symmetry from T to M. But magnetic frustration factors still keep increasing up to $x = 0.30$ due to short-range magnetic correlations. A detailed theoretical analysis of the exchange interactions with the help of crystal field theory in $Fe_{1-x}Cr_xVO_4$ on the basis of GKA rules of SE interactions in 180° octahedral configuration is discussed in the Appendix. For $x = 0.30$, the linear isotherm M-H curves are observed at 5 K and 22 K, indicating that there is no field-induced transition in conformity to the disappearance of spiral magnetic ordering, suggesting that the spiral spin structure gets suppressed and/or there is an increase in canting angle by Cr^{3+} doping into the system.

(d) $Fe_{1-x}Cr_xVO_4$ *($x = 0.5$, 0.66, and 0.75) (monoclinic + orthorhombic) phase.* Cr-rich samples of $Fe_{1-x}Cr_xVO_4$ between $x = 0.30$ and $x = 0.90$ compositions possess a mixed phase structure having both M and orthorhombic (O) symmetries. Figure S4 (Supplemental Material [42]) shows the DC magnetization as a function of temperature and the inverse magnetic susceptibility as a function of temperature where red solid lines represent the paramagnetic Curie-Weiss fit of $Fe_{1-x}Cr_xVO_4$ for $x = 0.50$, 0.66, and 0.75, respectively. The inset in Fig. S4 (Supplemental Material [42]) illustrates the first derivatives of M-T curves to find the Neel temperatures. An AFM transition in the magnetization curve is observed for $x = 0.50$ compound at 18 K, whereas no magnetic transition was observed in the measured temperature range, down to 5 K, for $x = 0.66$ and $x = 0.75$ compounds. The evaluated magnetic moment and frustration factor are given in Table I. The increasing content of Cr^{3+} in the compounds leads to

TABLE I. Obtained different magnetic parameters from χ^{-1} (T) plot of $Fe_{1-x}Cr_xVO_4$ ($0 \leqslant x \leqslant 1.0$) solid solutions.

Composition	$\theta_w(K)$	$T_{N1}(K)$	$T_{N2}(K)$	$T_R(K)$	$C = \Delta x/\Delta y$ $(K.emu/mol.Oe)$	$\mu_{\text{eff}} = \sqrt{8C}$ (μ_B)	$f = \mid \theta_w \mid /T_N$	$\chi = \frac{C}{T_N - \theta_w}$
$FeVO_4$	−109.74	21.85	15.65	....	4.49	5.99	5.022	0.03412
$Fe_{0.90}Cr_{0.10}VO_4$	−116.34	22.52	17.01	....	4.64	6.09	5.166	0.03340
$Fe_{0.825}Cr_{0.175}VO_4$	−137.21	23.03	21.05	....	4.24	5.82	5.957	0.02646
$Fe_{0.80}Cr_{0.20}VO_4$	−135.21	22.55	....	9.00	4.17	5.77	5.996	0.02643
$Fe_{0.70}Cr_{0.30}VO_4$	−126.65	21.03	....	12.00	3.81	5.52	6.022	0.02579
$Fe_{0.50}Cr_{0.50}VO_4$	−127.90	18.00	....	14.00	3.41	5.22	7.105	0.02337
$Fe_{0.10}Cr_{0.90}VO_4$	−222.04	43.29	....	20.00	3.24	5.09	5.129	0.01220
$CrVO_4$	−225.20	50.89	....	....	2.70	4.65	4.425	0.00978

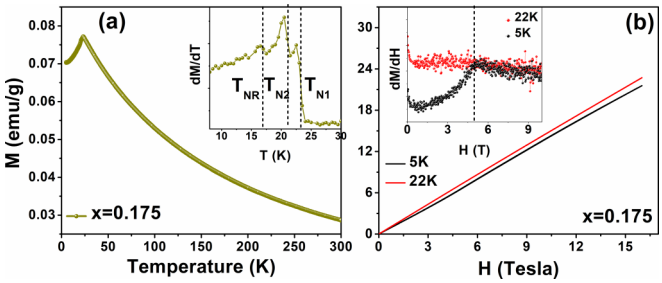

FIG. 7. (a) Magnetizations as a function of temperature at 500 Oe applied field of $Fe_{1-x}Cr_xVO_4$ solid solutions for $x = 0.175$ and (b) magnetization as a function of applied magnetic field. The inset in (a) illustrates the first derivatives of M-T curves to find the exact Neel temperatures and in (b) shows dM/dH to confirm nonlinearity.

short-range ordering with weak ferromagnetic nature due to d^5-d^3(Fe^{3+}-Cr^{3+}) interactions according to the GKA rule (as explained in the Appendix). The results are in conformity with earlier reports of Attfield *et al.* [40]. The M-H curves of the $x = 0.66$ sample recorded at 5K and 300K up to 16 T applied magnetic field. This curve shows dominated short-range ordering of weak ferromagnetic behavior at 5K and paramagnetic behavior at 300 K shown in Fig. S5 (Supplemental Material [42]).

(e) $Fe_{1-x}Cr_xVO_4$ *($x = 0.9$ and 1.0) orthorhombic phase.* The AFM transition temperature drastically increases to higher temperature for $x = 0.90$ and $x = 1.0$ which are found at 41.5 K and 71 K, respectively, with broad maxima related to short-range magnetic orderings [45,46,52]. For $x = 0.90$ and $x = 1.0$, there is a small bifurcation between ZFC and FC curves presented with different colors in Fig. 9(a), indicating spin canting associated with anisotropic energy [53] and the nature of magnetic transition is AFM as well. It is also observed that there is an upturn in magnetic moment in M-T curves around 20 K for $x = 0.90$, indicating the presence of weak ferromagnetic interaction corresponding to magnetic reorientation at that particular temperature due to higher Cr^{3+} substitution in Fe^{3+} sites and existing Fe-O-Cr interaction. The effective moment (μ_{eff} in μ_B) and magnetic frustration factors decrease continuously due to dominating d^3-d^3 (Cr-O-Cr) interaction with drastic changes in transition temperature

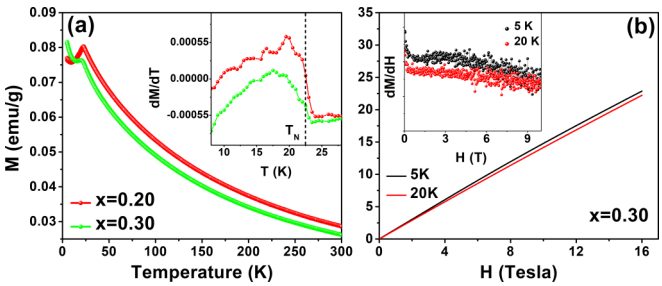

FIG. 8. Magnetizations as a function of temperature at 500 Oe applied field of $Fe_{1-x}Cr_xVO_4$ solid solutions for $x = 0.20$, 0.30, and (b) magnetization as a function of applied magnetic field for $x = 0.30$. The inset in (a) illustrates the first derivatives of M-T curves to find the exact Neel temperatures and in (b) shows dM/dH to confirm absence of nonlinearity.

toward higher temperatures. The M-H curve shows linear behavior at 5K and 30 K below the transition temperature (T_N) initially and an anomaly is observed at very high magnetic fields, indicating the field-induced transition in both the cases, shown in the dM/dH vs H curves of the inset of Figs. 9(b) and 9(c). And the high temperature M-H curves at 150 K and 300 K (above T_N) show linear paramagnetic behavior.

Figures 10(a) and 10(b) depict the magnetic phase diagram and the changes in effective moment and magnetic frustration factors with the increasing of Cr content in $Fe_{1-x}Cr_xVO_4$ ($0 \leqslant x \leqslant 1.0$) solid solutions and all the calculated parameters are given in Table I. Relative shifting between T_{N1} and T_{N2} is shown in the inset of Fig. 10(a). The T_{N2} shifts toward higher temperatures rapidly whereas the shifting of T_{N1} is rather slow. This leads to the proximity of these transitions in $x = 0.175$. However, the emergence of single transition beyond this composition is observed at lower temperatures than T_{N1} of $x = 0.175$. It further decreases for $x = 0.30$ and $x = 0.50$ but drastically increases at $x = 0.90$ and $x = 1.0$. The very complicated spin structure due to multiple magnetic interactions and its strong correlation with crystal structure makes these solid solutions an interesting problem in condensed-matter physics. A modest attempt to understand the magnetic lattice of these solid solutions is done through visualization of spiral spin network as in Fig. 11 and as explained in the next subsection in detail.

2. *Aspects of crystal structure and geometrical frustration, including spiral ordering in* $Fe_{1-x}Cr_xVO_4$

To understand the nature of magnetic interactions and magnetic frustration in $Fe_{1-x}Cr_xVO_4$, a detailed analysis based on the magnetic lattice arrangements in different crystallographic symmetries is given in detail. The crystal structures along with the nature of magnetic frustration in $Fe_{1-x}Cr_xVO_4$ are shown in Fig. 11.

(a) $Fe_{1-x}Cr_xVO_4$ *($x = 0.0$ and 0.10) triclinic phase.* $FeVO_4$ exhibits a special crystallographic feature with two FeO_6 octahedral and one trigonal bipyramidal FeO_5 polyhedrals where six Fe^{3+} ions (high spin state $S = 5/2$) are arranged in *S*-shaped clusters separated by $(VO_4)^{3-}$ groups consisting of two identical Fe_3O_{13} monomers [Fig. 11(d)]. These *S*-shaped clusters create frustrated magnetic units in $FeVO_4$. There are mainly two types of spin exchange interactions in TM-based vanadium oxides MVO_4 (M = Fe, Cr, In, Al, Bi, etc.), i.e., intrachain SE interactions of nearest-neighbor (NN) atoms through M-O-M path and interchain supersuperexchange (SSE) interactions between next-nearest-neighbor (NNN) atoms through M-O-V-O-M path. Figures 11(a) and 11(d) represent two types of magnetic interactions in $FeVO_4$: the intracluster SE and SSE and the intercluster SSE interactions linked with $(VO_4)^{3-}$ groups. Intercluster SSE interactions form triangular magnetic units as shown in Fig. 11(d) where one spin is frustrated. Hence, the geometrical magnetic frustration arises in the system due to the effective intracluster and intercluster Fe-Fe linkages forming a loop consisting of an odd number of Fe sites. The exact collinear AFM arrangements are not there due to magnetic frustration and spiral AFM arises at low temperature related to strong intercluster SSE interactions [38,54,55].

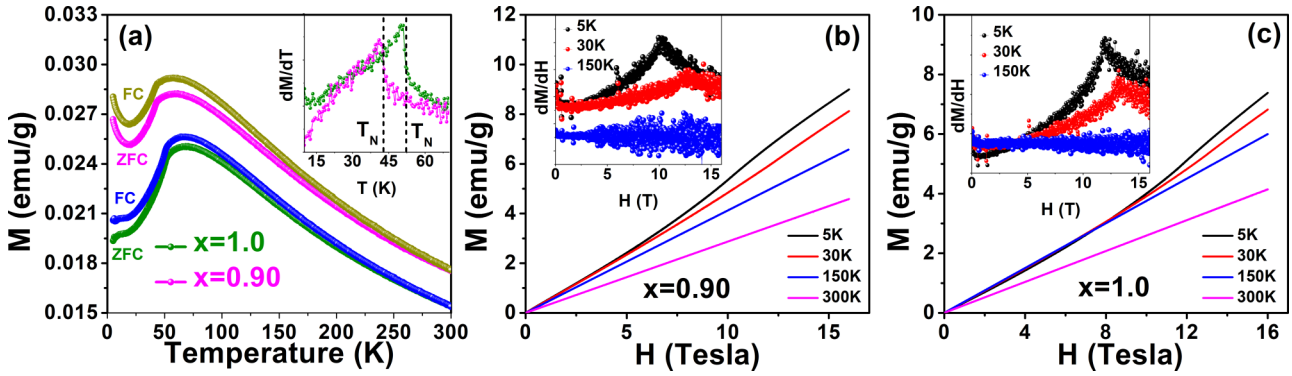

FIG. 9. Magnetizations as a function of temperature at 500 Oe applied field of $Fe_{1-x}Cr_xVO_4$ solid solutions for $x = 0.90$, 1.0, and magnetization as a function of applied magnetic field for (b) $x = 0.90$ and (c) $x = 1.0$. The inset in (a) illustrates the first derivatives of M-T curves to find the exact Neel temperatures and in (b) and (c) shows dM/dH to confirm nonlinearity.

(b) $Fe_{1-x}Cr_xVO_4$ *($x = 0.9$ and 1.0) orthorhombic phase.* The O $CrVO_4$ with *Cmcm* space group is having infinite chain of regular edge-shearing octahedrals of CrO_6 linked together by $(VO_4)^{3-}$ groups. The collinear AFM structures arise in $CrVO_4$ due to intrachain SE interactions of adjacent octahedral sites as shown in Fig. 11(c). The interchain SSE interactions are negligible compared with the intrachain SE interactions due to large spin-orbit interaction energy of the intrachain spin exchange path. The frustration of the interchain AFM interactions in the triangular arrangement of the CrO_4 chains is negligible as illustrated in Fig. 11(f) [54,56,57].

(c) $Fe_{1-x}Cr_xVO_4$ *($x = 0.30$) monoclinic phase.* In the solid-solution, Cr^{3+} incorporation at Fe sites in $Fe_{1-x}Cr_xVO_4$ leads to a crystal symmetry α-$MnMoO_4$-like structure with *C2/m* space group consisting of two Cr/FeO_6 octahedral crystal sites. Four edge-shearing octahedrals of two different sites make a parallelogram cluster linked with $(VO_4)^{3-}$ groups as shown in Fig. 11(b). The intracluster SE interactions between adjacent cation spins form a collinear AFM order while spin configuration of neighboring clusters will be frustrated where only four of the five AFM interactions are satisfied, shown in the Fig. 11(b). Here the exchange interactions are complicated and the frustrated magnetic order is observed due to the presence of additional d^3-d^3 and d^3-d^5 interactions. Intercluster SSE interactions between neighboring effective cluster spins results in a spiral AFM structure arising from large magnetic frustrations due to the near-triangular topology of AFM interactions between effective cluster spins through nonmagnetic $(VO_4)^{3-}$ groups, shown in Fig. 11(e) [40].

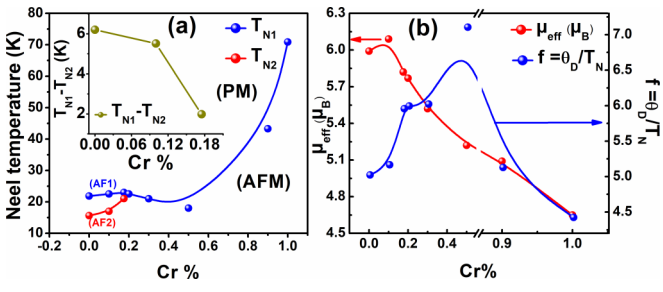

FIG. 10. (a) Magnetic phase diagram of $Fe_{1-x}Cr_xVO_4$ ($0 \leqslant x \leqslant 1.0$) solid solutions as a function of temperature. The inset presents the variation of the difference between two observed Neel temperatures as a function of compositions. (b) The variation of magnetic effective moment and frustration factors with compositions in $Fe_{1-x}Cr_xVO_4$ ($0 \leqslant x \leqslant 1.0$).

C. Temperature-dependent dielectric permittivity (ε) measurements in applied magnetic fields

1. Phase transitions in ε vs T in $Fe_{1-x}Cr_xVO_4$

Temperature-dependent dielectric measurements were carried out at different testing frequencies on $Fe_{1-x}Cr_xVO_4$ ($x = 0.0$, 0.10, 0.175, 0.20) systems under applied external magnetic fields. A detailed analysis of emergence of FE in different crystal symmetries is given below.

(a) $Fe_{1-x}Cr_xVO_4$ *($x = 0.0$ and 0.10) triclinic phase.* Figures 12(a) and 12(c) show variation of dielectric constants as a function of temperature at some selected frequencies for the compositions $x = 0.0$ and 0.10. It is clearly observed that there is significant dielectric anomaly with a sharp peak coinciding with the spiral magnetic transition temperature (T_{N2}) 15.64 and 17.02 K corresponding to the compositions $x = 0.0$, and 0.10, respectively. Evidently, these dielectric peaks are related to the emergence of improper ferroelectric order induced by noncollinear or spiral magnetic ordering, which get shifted to slightly higher temperatures, corresponding to the doping of Cr^{3+} contents in Fe^{3+} sites. In $FeVO_4$ systems, the magnetization-induced FE appears at 15.64 K, corresponding to noncollinear acentric magnetic structure arising due to antisymmetric spin-exchange interaction due to spin-orbit interactions within a network of strong inverse DM-type exchange interactions such as SE and SSE interactions. The SSE interaction pathways between NNN ions form *S*-shaped loops connecting an odd number of Fe^{3+} ions, indicating the geometrical and magnetic exchange frustrations, which play a crucial role in the chirality and FE. The first collinear acentric magnetic ordering does not show any FE at 21.8 K, though the inversion symmetry breaking of magnetic ordering occurs in both phases of $FeVO_4$, which is challenging the mechanism of the multiferroic behavior. Only frustrating AFM ordering (spiral) is the key of improper FE in pure $FeVO_4$. Here, Fe^{3+} - Fe^{3+} bipyramid symmetries may be introducing a strong frustrating AFM coupling along a particular direction of axis associated with microscopic

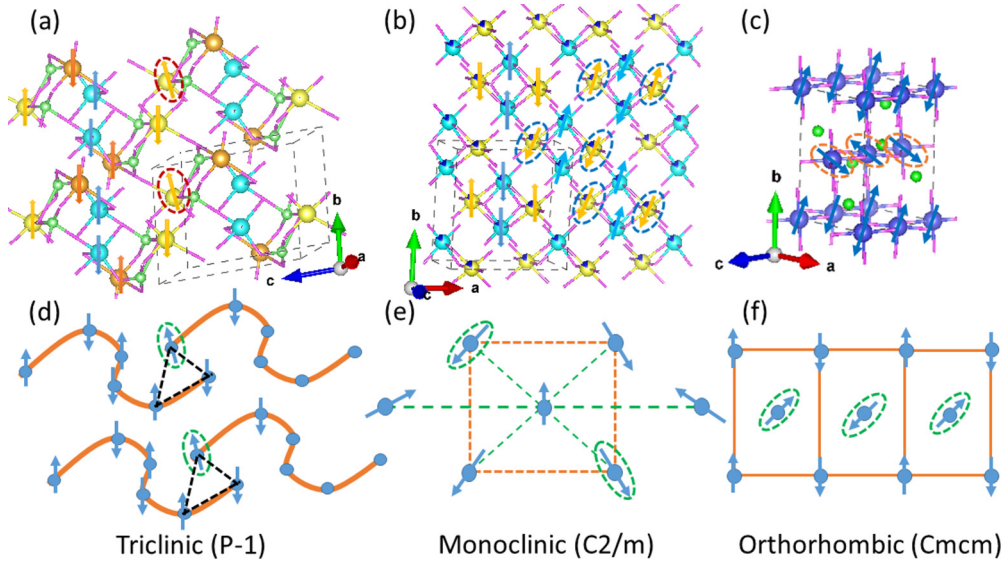

FIG. 11. Frustrated antiferromagnetic (AFM) spin arrangement and triangular geometry of magnetic frustration results in the helimagnetism in $Fe_{1-x}Cr_xVO_4$ solid solutions for (a), (d). Triclinic ($x = 0.0$); (b), (e) monoclinic ($x = 0.175$); and (c), (f) orthorhombic ($x = 1.0$) phases, respectively.

origin of spiral ordering which is caused by orientational long-range correlations and induced ferroelectric ordering at that particular magnetic ordering [58].

(b) $Fe_{0.825}Cr_{0.175}VO_4$ *(triclinic + monoclinic) phase.* Figure 13(a) shows the variation of temperature-dependent dielectric constant for the compositions $x = 0.175$ at some selected frequencies. A sharp peak at the spiral magnetic transition temperature (T_{N2}) 21.01 K is observed, corresponding to ferroelectric ordering. Unexpectedly, an additional dielectric anomaly is also identified at 17.02 K for $x = 0.175$ due to the presence of residual of T phase in the M phase, which is defined as T_{NR}. The ferroelectric transition is shifted to higher temperatures compared to T systems. However, this transition is a surprise to note here; hence there is no ferroelectric transition in M phase, as shown in the next subsection.

(c) $Fe_{1-x}Cr_xVO_4$ *($x = 0.30$) monoclinic phase.* Figure 14 shows the variation of temperature-dependent dielectric constant for the composition $x = 0.20$ where the dielectric anomaly disappeared in consonance of spiral order in this compound. In M systems, the coupling between Cr^{3+} and Fe^{3+} becomes stronger and suppresses the spiral spin structure. Hence, further increase of Cr^{3+} content beyond $x = 0.20$, the FE transition disappears with short-range magnetic correlations though the magnetic frustrations remain large. Since the strength of SSE interactions decreases with the Cr^{3+} doping, resulting from the overlap between $2p$ orbitals and metal orbitals, the large O–O distances decreases, which causes a weak AFM ordering associated with short-range magnetic correlations. The $Cr^{3+}(d^3)$-$Cr^{3+}(d^3)$ and $Fe^{3+}(d^5)$-$Cr^{3+}(d^3)$ interactions become dominating with the increasing Cr^{3+} content, show weak FM ordering [59–61], and suppress spiral ordering.

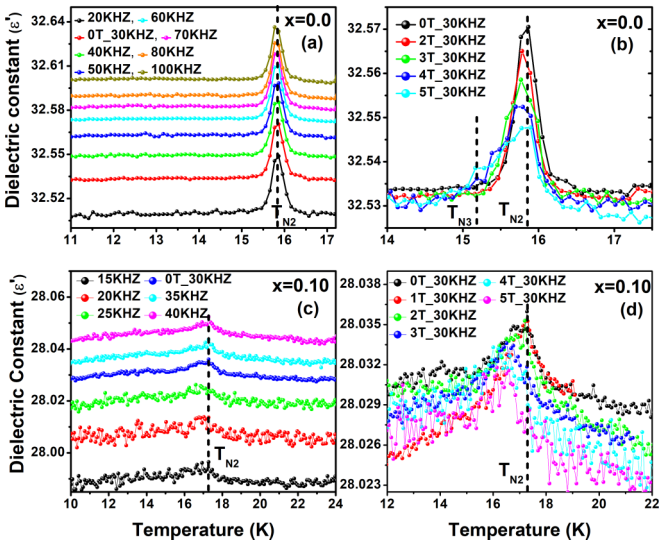

FIG. 12. The temperature-dependent dielectric constant of $Fe_{1-x}Cr_xVO_4$ at different testing frequencies in zero field (a) $x = 0.0$, (c) $x = 0.10$, and dielectric constant as a function of temperature in different applied magnetic fields (H = 0–5T), (b) $x = 0.0$, (d) $x = 0.10$.

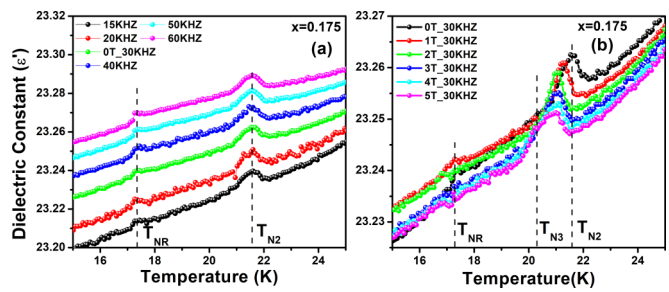

FIG. 13. The temperature dependence of the dielectric constant of $Fe_{1-x}Cr_xVO_4$ at different testing frequencies in zero field (a) $x = 0.175$ and the temperature dependence of dielectric constant in different applied magnetic fields (H = 0–5T) for (b) $x = 0.175$.

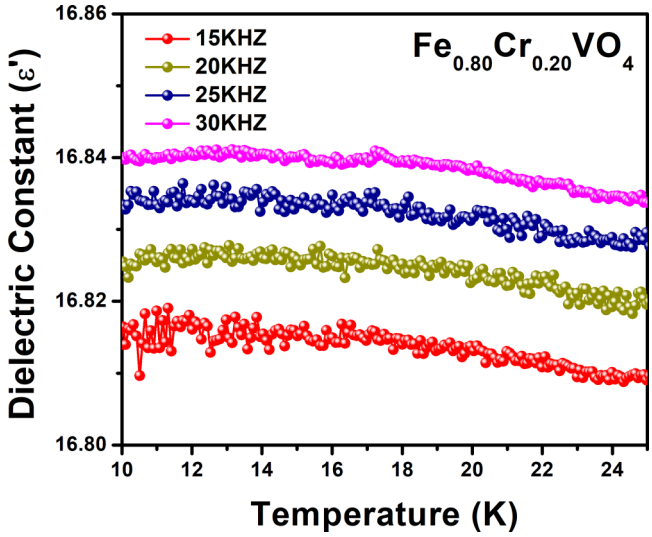

FIG. 14. The variation of temperature-dependent dielectric constant of $Fe_{1-x}Cr_xVO_4$ for the compositions (a) $x = 0.20$ in zero field.

2. *Magnetoelectric coupling in* $Fe_{1-x}Cr_xVO_4$

To investigate the ME coupling in $Fe_{1-x}Cr_xVO_4$ solid solutions, the temperature-dependent dielectric permittivity ε measurements at different external magnetic fields were also carried out. Figures 12(b), 12(d) and 13(b) show the variation of dielectric constants as a function of temperature at different magnetic fields for $Fe_{1-x}Cr_xVO_4$ solid solutions ($x =$ 0.0, 0.10, and 0.175), respectively. The dielectric anomaly corresponding to the ferroelectric order shifts toward lower temperatures and gets suppressed with broad peaks appearing with the increasing external magnetic fields.

Since the dielectric anomaly produced by ferroelectric ordering is associated with the acentric spiral magnetic structures, the reduction of transition temperatures in applied magnetic fields is expected and the suppressions in dielectric constants indicates the negative magnetodielectric characteristics of the materials. For $x = 0.175$ composition, the reduction of transition temperature with applied magnetic field is large as compared to pure $FeVO_4$ ($x = 0.0$) due to large magnetic frustration in this composition on account of the presence of residual T phase and emergence of short-range magnetic order.

The ME coupling is being quantified by calculating the magnetodielectric ratios or magnetocapacitance (MC); MC= $[\varepsilon'(H)\text{-}\varepsilon'(0)]/[\varepsilon'(0)] \times 100$, where, $\varepsilon'(H)$ and $\varepsilon'(0)$ represent the dielectric constants in the presence and absence of magnetic field, respectively [62]. Figure 15(a) demonstrates the variations of MC with the increase of Cr content at different external magnetic fields. It has been found that $\Delta\varepsilon_r$ decreases with the increasing applied magnetic fields, which signifies a negative coupling coefficient and the coupling become stronger at higher magnetic fields due to the field-induced ferroelectric ordering (T_{N3}). The absolute value of the MC experiences a continuous increase with an increase in the applied magnetic field and the curve of MC for $x = 0.175$ gradually becomes flat at higher fields, suggesting that MC gets saturated [63] as shown in inset of the Fig. 15(b). A multiferroic material gets strained under the influence of an

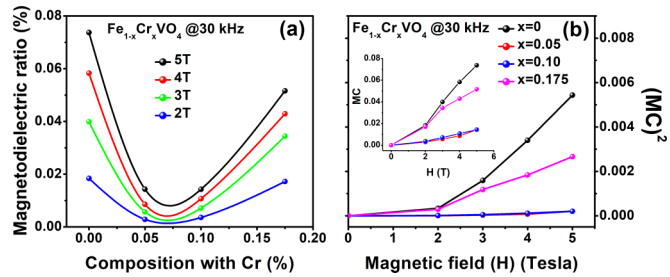

FIG. 15. Variation of magnetodielectric ratio (a) as a function of compositions at different external magnetic field and (b) as a function of applied magnetic field for different compositions of $Fe_{1-x}Cr_xVO_4$ ($x = 0.0$, 0.05, 0.10, and 0.175).

applied magnetic field, strain induces stress, which generates an electric field on ferroelectric domains; hence, the dielectric behavior is modified. It is clear from Fig. 15(b) of $(MC)^2$ vs H(T) plot that the relationship between $\Delta\varepsilon_r$ and H is approximately quadratic (beyond 2 T) and in the framework of the Ginzburg-Landau theory for the second-order phase transition; there exists an intrinsic quadratic ME coupling term, i.e., νP^2M^2 in free energy [64,65]. The origin of such a behavior has been predicted as a signature of coupling between magnetic and ferroelectric domains.

Another significant observation is being made in these results where a dielectric anomaly just below T_{N2} when the external applied field is strong (above 3 T) can be seen in Figs. 12(b) and 13(b). This newly emerging dielectric hump gradually increases with the increase in the magnetic field, eventually suppressing the dielectric constant at T_{N2}. This ferroelectric transition (at T_{N3}) is occurring above the field at which spin reorientation transitions were observed in M-H curve. The temperature dependence of the difference between dielectric constants of 0 T and 5 T applied magnetic fields is plotted for $Fe_{1-x}Cr_xVO_4$, which is considered to be proportional to the electromagnetic susceptibility of the materials, depicts a discontinuity at 15.65 K and 21.03 K corresponding to $x = 0.0$ and $x = 0.175$ composition, respectively, shown in Fig. 16(a) and 16(b). This discontinuity in electromagnetic susceptibility may be due to the competition between two magnetic phases at the particular region of the polar-nonpolar transition, indicating the magneto-dielectric coupling [35]. Another discontinuity at 15.10 K for $x = 0.0$ and at 20.01 K for $x = 0.175$ are observed in the polar AFM

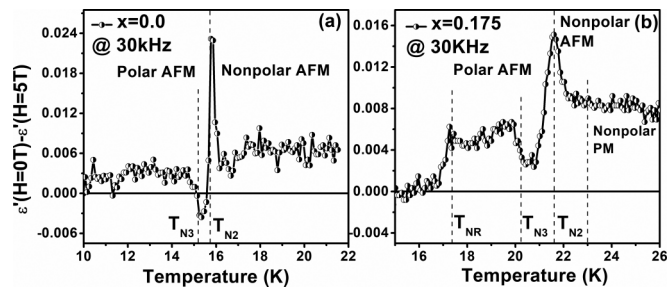

FIG. 16. Electromagnetic susceptibility of $Fe_{1-x}Cr_xVO_4$ solid solutions as a function of temperature for (a) $x = 0.0$ and (b) $x =$ 0.175.

region of curves which are just below T_{N2} transition indicating magnetic field induced multiferroic ordering at higher magnetic field (above 3 T). This discontinuity increases gradually with the increasing applied magnetic field. The multiferroic ordering at 17.02 K for $x = 0.175$ is also suppressed by applied magnetic field, shown in Fig. 16(b), associated with discontinuous behavior at 17.02 K. These observations are similar to that of other ME materials as reported in literature [6,66–68], confirming that the studied system exhibits ME behavior.

IV. SUMMARY AND CONCLUSIONS

In summary, magnetolattice coupling, magnetic frustration, and ME in $Fe_{1-x}Cr_xVO_4$ solid solutions is confirmed through temperature-dependent SXRD, temperature-, and magnetic-field-dependent DC magnetization and dielectric permittivity ε measurements. The lattice parameter anomalies across the magnetic transitions depict a strong coupling between lattice, spin, and charge degrees of freedom in these systems. Two AFM transitions evidenced at T_{N1} and T_{N2} in $FeVO_4$ correspond to collinear and noncollinear (spiral) incommensurate spin orderings respectively. Progressive substitution of Cr^{3+} ion into $Fe_{1-x}Cr_xVO_4$ generates additional magnetic-exchange interactions such as $Cr^{3+}(d^3)$-$Cr^{3+}(d^3)$ and $Fe^{3+}(d^5)$-$Cr^{3+}(d^3)$. These interactions are very weak in lower concentrations of Cr content (T region). The effective magnetic moment initially increases for $x = 0.10$ because of the presence of $Fe^{3+}(d^5)$-$Cr^{3+}(d^3)$ interactions with weak ferromagnetic nature in AFM structures, corresponding to the inverse DM antisymmetric exchange coupling. Further increase in the Cr content at the Fe site leads to the decrease in an effective magnetic moment associated with an average magnetic moment corresponding to dominating $Cr^{3+}(d^3)$-$Cr^{3+}(d^3)$ interactions. Magnetic frustration increases in the composition range $x = 0.175-0.30$ (M region) and for $x = 0.50$ (M + O region) with the suppression in spiral magnetic ordering due to increasing short-range magnetic correlations. With the increase of Cr concentrations above $x = 0.50$, the magnetic transition disappears down to 5 K for $x = 0.66$ and $x = 0.75$, samples suggesting that no long-range order is present for $x = 0.66$ and 0.75 due to significant short-range magnetic ordering. Further doping of Cr^{3+} ions leads to the increase in transition temperature to higher temperatures 41 K for $x = 0.90$ and 52 K for $x = 1.0$, associated with the reduction of magnetic frustration. The FE sustains up to $x = 0.175$ composition in the presence of spiral ordering and it disappears along with spiral structure for higher composition. The magnetic field dependence of the dielectric anomaly indicates the presence of ME coupling in the system at the spiral magnetic ordering as observed in the electromagnetic susceptibility curves having discontinuous behavior at transitions. The magnetic-field-induced mutiferroic transitions are identified below noncollinear magnetic order due to external field-induced spiral structures. The ME effect increases for the composition $x = 0.175$ due to increasing frustrated spiral magnetic order, where a small residual T phase coexists with M phase.

In conclusion, elaborate fingerprint studies on the origin of frustrated magnetism and ME effect and magneto-lattice coupling in $Fe_{1-x}Cr_xVO_4$ solid solutions were carried out through SXRD, temperature-, and field-dependent DC magnetization and dielectric constant measurements. The presence of highly frustrated magnetic phase disparate to the end members is found in $x = 0.175-0.30$ range (M region) in $Fe_{1-x}Cr_xVO_4$. It is confirmed from the DC magnetization studies that the two magnetic transitions (T_{N1}, T_{N2}) observed in $FeVO_4$ sustain fewer Cr concentration up to $x = 0.175$ (T and near M regions) and with the increase in Cr concentration beyond $x = 0.20$ (far M and O regions), the system shows single magnetic transition with a broad maxima. This is an indication to the suppression of the spiral magnetic ordering associated with the emergence of short-range magnetic correlation in $FeVO_4$ with the addition of Cr into the magnetic lattice. The measured effective magnetic moment slightly increases initially with the increase of Cr^{3+} content and then decreases systematically with further doping of Cr^{3+}. The magnetic frustration factor increases drastically in T and M phases and then decreases in O phase associated with short-range magnetic correlations. An observed anomaly in linear M-H isotherms with applied magnetic field below T_{N2} indicates field-induced spin-reorientation transitions at higher magnetic fields. In dielectric permittivity ε, a sharp peak at T_{N2} in T and at the boundary of T + M regions with a minimal suppression because of applied magnetic field is found and no such peak is observed in the far M phase. The observed FE at $x = 0.175$ in M symmetry, corresponding to the presence of the spiral magnetic at 17.02 K, needs further attention to understand its origin.

ACKNOWLEDGMENTS

G.R.T. and G.B. acknowledge UGC-DAE CSR, Indore and Mumbai center for financial support via No. CSR/CRS-87/2014-15/594 and No. UDCSR/MUM/CD/CRS-M-263/2017/1036, respectively. Authors thank Dr. V. Ganeshan and Dr. V. Siriguri of UGC-DAE CSR for their encouragement during the work. G.B. thanks Mr. Kranti Kumar Sharma for magnetization measurements. Authors from GGV, Bilaspur thank UGC and DST, Government of India, New Delhi for supporting Department of Pure and Applied Physics through UGC SAP DRS-I and FIST Level-I programs, respectively.

APPENDIX: EXCHANGE INTERACTIONS AND CRYSTAL FIELD THEORY IN $Fe_{1-x}Cr_xVO_4$

A thorough theoretical point of view is presented using crystal field theory and exchange interactions present in $Fe_{1-x}Cr_xVO_4$. The crystal field energy of degenerated d orbitals of TM splits in five subenergy states: $d_{x^2-y^2}$, d_{z^2}, d_{xy}, d_{yz}, and d_{zx}, caused by static electric field of surrounding ligand charge distributions. In octahedral field distributions with six ligand atoms, the d orbitals split into two sets of energy states with an energy difference Δoct (=10Dqoh) (octahedral splitting energy) where, $d_{x^2-y^2}$ and d_{z^2} are the higher energy states (e_g) and d_{xy}, d_{yz}, and d_{zx} are the lower energy states (t_{2g}). But in trigonal bipyramidal field distribution formed with five ligand atoms, the d orbitals split in three sets of energy states with two in lower energy states where d_{xy} and $d_{x^2-y^2}$ as first lower energy states (t_{2g1}) and d_{yz}, d_{zx} are second

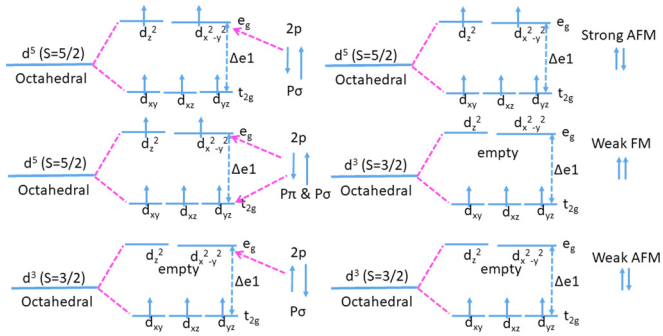

FIG. 17. Schematic representation of three different superexchange interactions corresponding to interactions between different clusters with d^5-d^5, d^5-d^3, and d^3-d^3 interactions in 180° octahedral configuration according to GKA rules.

lower energy states (t_{2g2}) and one higher energy state d_{z^2} (e_g). In an octahedral field, each higher energy state (e_g) has crystal field spitting energy (CFSE) 0.6Δoct and for each lower energy state (t_{2g}) it is -0.4Δoct to maintain the stabilization of energy of the center of gravity. But in trigonal bipyramid field, CFSE is $\sim 0.7\Delta$oct for single higher energy e_g state and for first lower t_{2g1} state it is $\sim 0.05\Delta$oct while that for second lower energy state is $\sim 0.25\Delta$oct. The electron distribution in these levels, according to their energy, depends upon the spin state of metal that is for high spin state the lower energy state t_{2g}, states half-filled first, then e_g state according to Hund's rule.

In $FeVO_4$, Fe^{3+} ions ($3d^5$, $L = 0$, $S = 5/2$) occupying the t_{2g^3} and e_g^2 electron configurations in two octahedral fields and t_{2g1^2}, t_{2g2^2}, and e_g^1 ($3d^3$, $S = 3/2$) occupying the t_{2g^3} electron configuration only where e_g state is empty.

In the octahedral field, for Fe^{3+} ions the SE and SSE interactions with NN and NNN Fe^{3+} ions through Fe^{3+}-O-Fe^{3+} and Fe^{3+}-O-V-O-Fe^{3+} paths, respectively, brought by strong spin-orbit-exchange interactions within TM (Fe^{3+}) t_{2g} orbitals or between t_{2g} and e_g orbitals while the spin-orbit

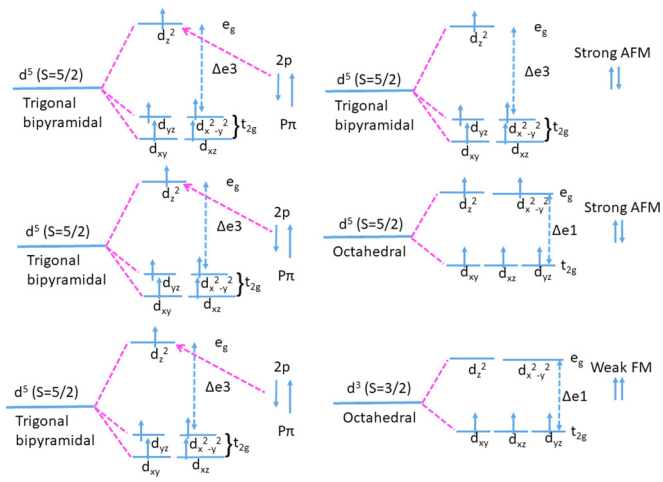

FIG. 18. Schematic representation of three different superexchange interactions corresponding to interactions between different clusters with d^5-d^5, d^5-d^3, and d^3-d^3 interactions in 180° trigonal bipyramidal configuration, according to GKA rules.

Unpaired outer most electrons hybridizations in 180° octahedral configurations.	Super-superexchange interactions (NNN)		Superexchange interactions (NN)		Final State
	pσ	pπ	pσ	pπ	
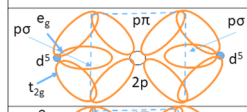	strong	Weak	Strong	Weak	Strong
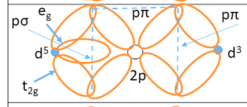	moderate	weak	moderate	Weak	Weak
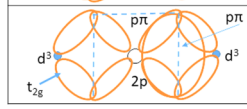	Weak to moderate	weak	.....	weak	Weak

FIG. 19. Three possible 180° M-O-M interactions between octahedral-site cations according to GKA rules of superexchange interactions.

interaction between t_{2g} and e_g is less in trigonal bipyramid field due to large CFSE. These types of spin-exchange interactions promote AFM ordering of spin at low temperature and noncollinear AFM ordering produced by the typical loops, like the structure connecting the odd number of Fe^{3+} ions in the interaction paths [38]. For Cr^{3+} ions in octahedral field neglecting the spin orbit coupling to t_{2g} orbital state in these SE and SSE interactions while the empty e_g state occupy orbitally nondegenerate [69].

So, according to crystal field theory, crystal field stabilization energy for $3d^3$ Cr^{3+} increases while the high spin $3d^3$ Fe^{3+} does not in a regular octahedral field. The theoretical effective moment obtained from the spin-only formula $\mu_{\text{eff}} = 2\sqrt{S(S+1)}$, where S is the spin state, for Fe^{3+} ($L = 0$, $S = 5/2$), $\mu_{\text{eff}} = 5.91\ \mu_B$, and for Cr^{3+}($S = 3/2$) it is $3.87\ \mu_B$ [69]. When Fe^{3+} ions are substituted by Cr^{3+} ions in $FeVO_4$, then the ordering of both ions in between different sites depends upon the sizes and the electronic configuration of the cations. Therefore, with increasing Cr^{3+} content, a very small degree of Cr/Fe ordering reflects the electronic differences between Fe^{3+} and Cr^{3+} and also significant differences between Cr/Fe(1)-O and Cr/Fe(2)-O bond distances. The distortions in the octahedral symmetry (Oh) are due to edge sharing within the crystal sites (clusters) and Cr^{3+} ions can get a more regular environment in the less edge-sharing cluster easily. Since the strength of intrachain (SE) and interchain (SSE) interactions of a magnetic orbital depends upon the increasing or decreasing overlap between $2p$ orbitals in the short or long M-O bonds and O–O contacts, respectively.

Therefore, in the $Fe_{1-x}Cr_xVO_4$ ($0 \leqslant x \leqslant 1.0$) solid solutions, the spin-exchange interactions are complicated due to the average magnetic order of all the possible sites with three different interactions present in the system together like d^5-d^5, d^5-d^3, and d^3-d^3 interactions. According to the GKA rules, a 180° SE (the magnetic ion-ligand-magnetic ion angle is 180° of two magnetic ions with partially filled d shells) is strongly AFM, whereas a 90° SE interaction is ferromagnetic and much weaker. In octahedral configurations, the $Fe^{3+}(d^5)$-O-$Cr^{3+}(d^3)$ would show a very weak ferromagnetic behavior according to the GKA rules [56–58].

Figure 17 shows three different SE interactions corresponding to interactions between different clusters with d^5-d^5, d^5-d^3, and d^3-d^3 interactions in octahedral configuration (similar to the trigonal bipyramidal configuration shown in Fig. 18). It is observed that the spin-exchange interactions are stronger for $Fe^{3+}(d^5)$ where σ and π SE interactions are present, which are strong AFM in nature, while that for $Cr^{3+}(d^3)$ are less stronger than $Fe^{3+}(d^5)$ where only π SE interactions are present and d^5-d^3 interactions are weakly FM in nature due to some weak or moderate and SE interactions according to GKA rules, shown in Fig. 19 in a 180° M-O-M SE interaction between octahedral sites clusters. So, in $Fe_{1-x}Cr_xVO_4$ ($0 \leqslant x \leqslant 1.0$) solid solutions, the effective magnetic moment (μ_{eff}) will be the average over contributions of all the interactions with d^5-d^5, d^5-d^3, and d^3-d^3 interactions, i.e., $\mu_{\text{eff}} = \sqrt{[(1-x)Fe^{3+} + xCr^{3+} + \Delta(Fe^{3+}..Cr^{3+})]}\ \mu_B$ unit.

[1] S. Dong, J.-M. Liu, S.-W. Cheong, and Z. Ren, Adv. Phys. **64**, 519 (2016).
[2] J. F. Scott, Nat. Mater. **6**, 256 (2007).
[3] S.-W. Cheong and M. Mostovoy, Nat. Mater. **6**, 13 (2007).
[4] C. N. R. Rao, A. Sundaresan, and R. Saha, J. Phys. Chem. Lett. **3**, 2237 (2012).
[5] D. M. Juraschek, M. Fechner, A. V. Balatsky, and N. A. Spaldin, Phys. Rev. Mater. **1**, 014401 (2017).
[6] W. Eerenstein, N. D. Mathur, and J. F. Scott, Nature **442**, 759 (2006).
[7] C. N. R. Rao and C. R. Serrao, J. Mater. Chem. **17**, 4931 (2007).
[8] M. Mostovoy, Phys. Rev. Lett. **96**, 067601 (2006).
[9] Y. J. Choi, H. T. Yi, S. Lee, Q. Huang, V. Kiryukhin, and S. W. Cheong, Phys. Rev. Lett. **100**, 047601 (2008).
[10] D. Khomskii, Physics **2**, 20 (2009).
[11] J. van den Brink and D. Khomskii, J. Phys.: Condens. Matter **20**, 434217 (2008).
[12] C. Lu and J.-M. Liu, J. Materiomics **2**, 213 (2016).
[13] M. Fiebig, T. Lottermoser, D. Meier, and M. Trassin, Nat. Rev. Mater. **1**, 16046 (2016).
[14] Y. Tokura, S. Seki, and N. Nagaosa, Rep. Prog. Phys. **77**, 076501 (2014).
[15] N. Zhang, S. Dong, and J.-M. Lui, Front. Phys. **7**, 408 (2012).
[16] H. J. Xiang, S.-H. Wei, M. H. Whangbo, and J. L. F. D. Silva, Phys. Rev. Lett. **101**, 037209 (2008).
[17] G. Lawes, A. B. Harris, T. Kimura, N. Rogado, R. J. Cava *et al.*, Phys. Rev. Lett. **95**, 087205 (2005).
[18] L. C. Chapon, P. G. Radaelli, G. R. Blake, S. Park, and S. W. Cheong, Phys. Rev. Lett. **96**, 097601 (2006).
[19] K. Taniguchi, N. Abe, T. Takenobu, Y. Iwasa, and T. Arima, Phys. Rev. Lett. **97**, 097203 (2006).
[20] A. H. Arkenbout, T. T. M. Palstra, T. Siegrist, and T. Kimura, Phys. Rev. B **74**, 184431 (2006).
[21] T. Kimura, G. Lawes, T. Goto, Y. Tokura, and A. P. Ramirez, Phys. Rev. B **71**, 224425 (2005).
[22] Y. Yang, H. Xiang, H. Zhao, A. Stroppa, J. Zhang, S. Cao, J. Iniguez, L. Bellaiche, and W. Ren, Phys. Rev. B **96**, 104431 (2017).
[23] S. Hu, L. Chen, Y. Wu, L. Yu, X. Zhao, S. Cao, J. Zhang, and W. Ren, Chin. Sci. Bull. **59**, 5170 (2014).
[24] Y. J. Guo, S. Dong, K. F. Wang, and J. M. Liu, Phys. Rev. B **79**, 245107 (2009).
[25] F. K. Chiang, M. W. Chu, F. C. Chou, H. T. Jeng, H. S. Sheu, F. R. Chen, and C. H. Chen, Phys. Rev. B **83**, 245105 (2011).
[26] N. Lee, Y. J. Choi, M. Ramazanoglu, W. Ratcliff, V. Kiryukhin, and S. W. Cheong, Phys. Rev. B **84**, 020101(R) (2011).
[27] G. Sharma, J. Saha, S. D. Kaushik, V. Siruguri, and S. Patnaik, Appl. Phys. Lett. **103**, 012903 (2013).
[28] J. Blasco, J. L. Garcia-Munoz, J. Garcia, G. Subais, J. Stankiewcz, J. A. Rodriguez, and C. Ritter, Phys. Rev. B **96**, 024409 (2017).
[29] H. Murakawa, Y. Onose, S. Miyahara, N. Furukawa, and Y. Tokura, Phys. Rev. Lett. **105**, 137202 (2010).
[30] H. Katsura, N. Nagaosa, and A. V. Balatsky, Phys. Rev. Lett. **95**, 057205 (2005).
[31] D. Kobayashi, T. Yoshikawa, M. Matsuo, R. Iguchi, S. Maekawa, E. Saitoh, and Y. Nozaki, Phys. Rev. Lett. **119**, 077202 (2017).
[32] K. Hemamoto, M. Ezawa, Kun W. Kim, T. Morimoto, and N. Nagaosa, Phys. Rev. B **95**, 224430 (2017).
[33] F. Nichele, S. Hennel, P. Pietsch, W. Wegscheider, P. Stano, P. Jacquod, T. Ihn, and K. Ensslin, Phys. Rev. Lett. **114**, 206601 (2015).
[34] A. Dixit, G. Lawes, and A. B. Harris, Phys. Rev. B. **82**, 024430 (2010).
[35] B. Kundys, C. Martin, and C. Simon, Phys. Rev. B **80**, 172103 (2009); L. Zhao, M. P. Y. Wu, K.-W. Yeh, and M.-K. Wu, Solid State Commun. **151**, 1728 (2011).
[36] A. Dixit and G. Lawes, J. Phys.: Condens. Matter **21**, 456003 (2009).
[37] J. Zhang, L. Ma, J. Dai, Y. P. Zhang, Z. He, B. Normand, and W. Yu, Phys. Rev. B **89**, 174412 (2014).
[38] A. Daoud-Aladine, B. Kundys, C. Martin, P. G. Radaelli, P. J. Brown, C. Simon, and L. C. Chapon, Phys. Rev. B **80**, 220402(R) (2009).
[39] A. Kumarasiri, E. Abdelhamid, A. Dixit, and G. Lawes, Phys. Rev. B **91**, 014420 (2015).
[40] J. P. Attfield, A. K. Chertham, D. C. Johnson, and T. Novet, J. Mater. Chem. **1**, 867 (1991).
[41] G. Bera, V. R. Reddy, P. Rambabu, P. Mal, P. Das, N. Mohapatra, G. Padmaja, and G. R. Turpu, J. Appl. Phys. **122**, 115101 (2017).
[42] See Supplemental Material at http://link.aps.org/supplemental/10.1103/PhysRevB.100.014436 for additional data.
[43] M. Suzuki and I. S. Suzuki, Lecture note on solid state physics superexchange interaction (Binghamton, New York, 2009).
[44] J. B. Goodenough, Scholarpedia **3**, 7382 (2008).
[45] A. P. Ramirez, Annu. Rev. Mater. Sci. **24**, 453 (1994).
[46] A. A. Belik, M. Azuma, and M. Takano, Inorg. Chem. **42**, 8572 (2003).
[47] A. N. Vasilev, L. A. Ponomarenko, E. V. Antipov, Yu. A. Velikodny, A. I. Smirnov, M. Isobe, and Y. Ueda, Physica B (Amsterdam) **284–288**, Part 2, 1615 (2000).
[48] M. A. McGuire and V. O. Garlea, Phys. Rev. B **93**, 054404 (2016).

[49] K. Yadav, M. P. Singh, F. S. Razavi, and G. D. Varma, Mater. Res. Express **4**, 076102 (2017).
[50] L. I. Zawislak, G. L. F. Fraga, J. B. Marimon da Cunha, D. Schmitt, A. S. Carrico, and C. A. dos Santos, J. Phys.: Condens. Matter **9**, 2295 (1997).
[51] L. Yung, K. Huang, C. Hou, W. Feng, S. Wang, C. Zhou, and S. Feng, New J. Chem. **38**, 1168 (2014).
[52] J. E. Greedan, N. P. Raju, and I. J. Davidson, J. Solid State Chem. **128**, 209 (1997).
[53] N. Guskos, G. Zolnierkiewicz, M. Pilarska, J. Typek, A. Blonska-Tabero, and C. Aidinis, Acta Phys. Pol. A **132**, 24 (2017).
[54] H.-J. Koo, M. H. Whangbo, and K. S. Lee, Inorg. Chem. **42**, 5932 (2003).
[55] K. Liu, Y. Hou, X. Gong, and H. Xiang, Nat. Sci. Rep. **6**, 19653 (2016).
[56] E. J. Baran, J. Mater. Sci. **33**, 2479 (1998).
[57] P. R. Elliston, Can. J. Phys. **47**, 1865 (1969).
[58] A. Scaramucci, H. Shinaoka, M. V. Mostovoy, M. Muller, C. Mudry, M. Troyer, and N. A. Spaldin, Phys. Rev. X **8**, 011005 (2018).
[59] Y. Qiao, Y. Zhou, S. Wang, L. Yuan, Y. Du, D. Lu, G. Che, and H. Chef, Dalton Trans. **46**, 5930 (2017).
[60] N. M. Murari, R. Thomas, A. Winterman, R. E. Melgarejo, S. P. Pavunny, and R. S. Katiyar, J. Appl. Phys. **105**, 084110 (2009).
[61] Y. Zhou, R. Zhang, Y. Fan, Z. Wang, W. Mao, J. Zhang, Y. Min, J. Yang, Y. Pu, and X. Li, Solid State Commun. **270**, 12 (2018).
[62] N. Adhlakha and K. L. Yadav, J. Mater. Sci. **49**, 4423 (2014).
[63] N. Adhlakha, K. L. Yadav, and R. Singh, Smart Mater. Struct. **23**, 105024 (2014).
[64] T. Kimura, S. Kawamoto, I. Yamada, M. Azuma, M. Takano, and Y. Tokura, Phys. Rev. B **67**, 180401(R) (2003).
[65] Y.-K. Jun, S. B. Lee, M. Kim, S.-H. Hong, J. W. Kim, and K. H. Kim, J. Mater. Res. **22**, 3397 (2007).
[66] B. Kundys, A. Maignan, D. Pelloquin, and Ch. Simon, Solid State Sci. **11**, 1035 (2009).
[67] N. Ortega, A. Kumar, J. F. Scott, and R. S. Katiyar, J. Phys.: Condens. Matter **27**, 504002 (2015).
[68] J. P. Rivera, H. Schmid, J. M. Moret, and H. Bill, Int. J. Magnetism **6**, 211 (1974).
[69] N. Elliott, J. Chem. Phys. **46**, 1006 (1967).